Research Article | Vol. 11, No. 8 / 1 August 2020 / Biomedical Optics Express 4255
Biomedical Optics EXPRESS

Methylene blue-filled biodegradable polymer particles as a contrast agent for optical coherence tomography

JORGE A. PALMA-CHAVEZ,[1] WIHAN KIM,[2] MICHAEL SERAFINO,[3] JAVIER A. JO,[3] PHAPANIN CHAROENPHOL,[4] AND BRIAN E. APPLEGATE[2,5,*]

[1]Department of Biomedical Engineering, Texas A&M University, College Station, TX 77843, USA
[2]Department of Otolaryngology–Head and Neck Surgery, University of Southern California, Los Angeles, CA 90033, USA
[3]Department of Electrical and Computer Engineering, University of Oklahoma, Norman, OK 73019, USA
[4]Department of Mechanical Engineering, Texas A&M University, College Station, TX 77843, USA
[5]Department of Biomedical Engineering, University of Southern California, Los Angeles, CA 90089, USA
*brianapp@usc.edu

Abstract: Optical coherence tomography (OCT) images largely lack molecular information or molecular contrast. We address that issue here, reporting on the development of biodegradable micro and nano-spheres loaded with methylene blue (MB) as molecular contrast agents for OCT. MB is a constituent of FDA approved therapies and widely used as a dye in off-label clinical applications. The sequestration of MB within the polymer reduced toxicity and improved signal strength by drastically reducing the production of singlet oxygen and leuco-MB. The former leads to tissue damage and the latter to reduced image contrast. The spheres are also strongly scattering which improves molecular contrast signal localization and enhances signal strength. We demonstrate that these contrast agents may be imaged using both pump-probe OCT and photothermal OCT, using a 830 nm frequency domain OCT system and a 1.3 μm swept source OCT system. We also show that these contrast agents may be functionalized and targeted to specific receptors, e.g. the VCAM receptor known to be overexpressed in inflammation.

1. Introduction

Methylene blue (MB) has been used clinically for over a century and is a constituent of several therapies that have had FDA approval. It's deep blue color makes it readily visible to the unaided eye and it's photophysics support imaging with a variety of optical imaging modalities [1–3], including optical coherence tomography [4]. We recently demonstrated in vivo pump-probe optical coherence tomography (PPOCT) imaging of the protokidneys in a zebrafish passively tagged with MB [5]. Nevertheless, issues remain for this versatile multimodal contrast agent to find regular use. When illuminated with visible light, MB can enter a metastable triplet state that when quenched by oxygen, produces singlet oxygen radical which causes cellular damage [6]. Roughly half of the methylene blue in vivo is reduced to leuco-MB, a colorless variant not suitable as a contrast agent [7]. It has negligible scattering, hence relying on intrinsic scattering for observation. Functionalization for active tagging runs the risk of altering the photophysics that make it such a versatile contrast agent.

We have sought to address these issues by developing a contrast agent with MB encapsulated in micro- or nano-particles of poly lactic-co-glycolic acid (PLGA), a biodegradable polymer. PLGA is well suited for this application since it is FDA approved for various applications including drug delivery, hence we expect the resulting MB-PLGA contrast agent to have few side effects and be safe for use in animals and likely humans. Hence the regulatory pathway may be less arduous.

#399322 https://doi.org/10.1364/BOE.399322
Journal © 2020 Received 5 Jun 2020; revised 30 Jun 2020; accepted 6 Jul 2020; published 10 Jul 2020

Biomedical Optics EXPRESS

While MB-PLGA particles could be imaged using various optical approaches, we are interested in its use as a contrast agent for optical coherence tomography (OCT). OCT is widely used in research and clinical applications to get high-resolution cross-sectional images of various biological samples [8–13]. In OCT, the image contrast is derived from variations of refractive index which provides a measure of tissue morphology. Unfortunately, very little information on the biomolecular environment is carried by the standard OCT image. Efforts to incorporate molecular contrast into OCT include two techniques that alternately exploit transient absorption and localized heating to engender a time-dependent modulation of the OCT signal.

The two approaches, labeled pump-probe OCT (PPOCT) and photothermal OCT (PTOCT), require an amplitude modulated excitation laser (pump laser), resonant with an absorption band of the target contrast agent. This in addition to an otherwise typical OCT system, hence the optical system requirements for both are largely identical. PPOCT incorporates the principles of pump-probe spectroscopy and requires a second absorption resonance at the wavelength of the OCT light source (see [14,15] for more details). Absorption of the pump laser generates a transient absorption of the OCT light, hence amplitude modulation of the pump laser leads to an amplitude modulation of the OCT signal. In PTOCT the absorption of the pump laser leads to localized heating. Pump laser modulation leads to a modulation of the local refractive index, hence a modulation of the phase of the OCT signal. In both, the modulation of the OCT signal is frequency encoded at the pump laser modulation frequency.

Herein we report on the development of a synthetic route to generate both nano- and microparticles of PLGA filled with aqueous MB. We report on the physical properties of the resulting contrast agents and demonstrate PPOCT and PTOCT imaging at 830 nm and PTOCT at 1310 nm. 830 and 1310 nm are two of the most widely used OCT wavelengths.

2. Materials and methods

2.1. Nano-/microparticle synthesis

Poly lactic-co-glycolic acid (PLGA) (50:50 and 75:25) were acquired from Evonik Industries. Poly ethylene-maleic acid (PEMA), poly vinyl alcohol (PVA), Dulbecco's phosphate buffered saline (DPBS), N-(3-Dimethylaminopropyl)-N′-ethyl carbodiimide (EDAC), reduced dipotassium salt (NADH) and diaphorase from *Clostridium Kluyveri* (NADH dehydrogenase) were purchased from Sigma-Aldrich. NeutrAvidin protein was acquired from Thermo-Fisher. Biotinylated vascular cell adhesion molecule 1 (VCAM-1) antibodies were purchased from Abcam. Methylene blue was obtained from Fisher Scientific. All reagent grade organic solvents were purchased from VWR.

MB-PLGA particles were fabricated by an oil-in-water (O/W) emulsion solvent evaporation method [16–18]. Briefly, an oil phase was prepared by dissolving 0.05-0.1 mg/mL of methylene blue and 2.5-10 mg/mL of PLGA polymer in dichloromethane (DCM). Then, the oil phase was injected dropwise into a continuous water phase containing 3% of poly-vinyl alcohol (PVA) and poly-ethylene-maleic acid (PEMA) dissolved in deionized water (DI water). Water phase pH was adjusted using a sodium hydroxide solution (2M NaOH). PVA acts as a polymer stabilizer, stabilizing the droplets and preventing particles from aggregating. PEMA increases the number of carboxyl groups on the particle surface, increasing available active sites for ligand functionalization [19]. During the emulsification process, the oil phase was broken into small droplets by shear stress produced either by a magnetic stir plate (Isotemp, Fisher Scientific) for microparticles or a 20 kHz sonicator tip (Q125, QSonica) for nanoparticles. The emulsion mixture was stirred under a fume hood for 3 hours to ensure complete organic solvent evaporation and allow particles to solidify. The particles were washed, collected via centrifugation, and lyophilized (Freezone 2.5, LABCONCO). The dried MB-loaded particles were stored at -20°C in the dark until use. Relevant parameters used to prepare PLGA particles in this study are summarized in Table 1.

Biomedical Optics EXPRESS

Table 1. Fabrication parameters optimized to form MB loaded PLGA particles of the intended average diameters.

Parameter	Microparticles	Nanoparticles
Shear Stress	Stir plate (1200 rpm)	1/8" Sonicator Tip (30kHz, ~25 W)
Polymer Concentration	2 mg/ml	1 mg/ml
Emulsion Volume	90 ml	10 ml
Reactor Volume	200 ml	25 ml
Intended Diameter	2-5 μm	80-100 nm

2.2. Nano-/microparticle characterization

Particle size and count were determined using a bright field microscope (Eclipse 80i, Nikon) and a nanoparticle tracking analysis system (NanoSight LM10, Malvern Instruments). Particle surface charge was measured by zeta potential (Zetasizer Nanoseries, Malvern Instruments). Morphology of the PLGA particles was verified by scanning electron microscopy (SEM Neoscope JCM-5000, Nikon). Methylene blue encapsulation efficiency of PLGA particles was determined by measuring light absorption at 665 nm and comparing against solutions of known MB concentration using a microplate reader (Synergy HTX, BioTek). MB encapsulation efficiency was defined as the ratio of total MB obtained from dissolved particles divided by the initial amount of MB used during the particle fabrication process. Release rate of MB was determined by incubating PLGA particles in phosphate buffered saline at 37°C and periodically measuring the amount of released MB in the supernatant via spectrometry (Synergy HTX, BioTek).

Protection of methylene blue from enzymatic reduction was tested by a method previously reported [20–22]. Briefly, MB loaded PLGA particles and free soluble MB were prepared in 3 mL of Dulbecco's phosphate buffered saline (DPBS) (pH 7.4). NADH and diaphorase (NADH dehydrogenase), an enzyme present in red blood cells capable of reducing MB in vivo [23,24], were sequentially added into the samples. Fluorescence intensity of MB at 680 nm was monitored for 1 hour using a photon-counting spectrofluorimeter (PC1, ISS). The fluorescence intensity of these solutions without NADH and diaphorase was used as a control.

The generation of singlet oxygen by MB-PLGA spheres, was verified using the Anthracene-9, 10-dipropionic acid disodium salt (ADPA) method previously described [20]. MB loaded PLGA particles and free soluble MB were prepared in 2 mL of DPBS (pH 7.4) and mixed with 100 μM of ADPA, a singlet oxygen quencher commonly used to detect free radicals in a solution. The MB solutions were illuminated with our pump light source at 663 nm (2.5 mW) and samples were periodically collected for up to 30 minutes. The fluorescence emission spectra of ADPA under excitation at 378 nm, was measured using a photon-counting spectrofluorimeter (PC1, ISS).

PLGA particles were labeled with targeting ligands via EDAC-carbodiimide and avidin-biotin linkages as previously described [25]. Briefly, carboxylated PLGA spheres were initially modified with NeutrAvidin proteins in EDAC and MES buffer. Subsequently, biotinylated human VCAM-1 antibody was added to PLGA micro and nanoparticles. Functionalized particles were washed in DPBS, collected by centrifugation, and stored at 4°C in the dark until use. The coverage density of VCAM-1 antibodies on the microparticle surface was measured by flow cytometry (FACSCalibur, Becton, Dickinson and Company). Microparticles were stained with FITC-labeled rabbit anti-Mouse IgG (H + L) secondary antibodies. Non-stained aVCAM-1 microparticles, avidin-coated microparticles stained with the secondary antibodies and aVCAM-1 microparticles stained with isotype controls were used as controls. Similarly, functionalization of PLGA nanoparticles was evaluated by an ELISA assay. Avidin conjugated PLGA nanoparticles were incubated with biotin-labeled horseradish peroxidase (B-HRP) for 30 min. Particles were then washed with PBS to remove unbounded B–HRP and then transferred into an opaque 96-well plate.

Biomedical Optics EXPRESS

Amplex red fluorescent peroxidase was added to samples, allowing for a 10-min reaction [26]. The fluorescent intensity of untreated (control) and Amplex red treated particles was measured using a microplate reader (Synergy HTX, BioTek). The number of functionalized micro and nanoparticles was fixed matching their total volume (carrying similar total MB mass) to fairly compare their site density.

2.3. Molecular contrast imaging

Two different OCT imaging systems were used to assess the utility of the contrast agent, a frequency domain OCT (FD-OCT) at 830 nm and a Swept Source OCT (SS-OCT) at 1.3μm. In both imaging systems a pump-probe approach was implemented to monitor pump induced variations in the local optical properties due to the presence of encapsulated MB. The pump light source for both systems was a 663 nm diode laser (Toptica, iBeam Smart PT660). Amplitude modulated light from this laser was combined with the respective sample arms via a dichroic mirror. The FD-OCT system, with axial and lateral resolutions of 7.6 μm and 19 μm respectively (in air), has been described previously in [27] and [5]. Briefly, a super luminescent diode (SLD) centered at 830 nm with a ~40 nm bandwidth was used as the probe and typical OCT light source. The probe light was launched into a 2×2 fused fiber coupler to form a Michelson interferometer. Pump and probe were focused to a spot diameter of 19 μm and the sample was laterally scanned by a pair of galvo mirrors. A custom spectrometer was used as a detector. The SS-OCT system was one we typically use for cochlear vibrometry on small animals first described in [28] but updated over the years (see for instance [29] and references therein). The system is designed to have high phase-stability which is crucial for PTOCT. Recent improvements include the addition of a Vernier-tuned distributed Bragg reflector swept laser [30] at 1310 nm (Insight) with 92.6 nm bandwidth utilizing a Mach-Zehnder type interferometer as described in [31], with axial and lateral resolutions of 9.8 μm and 18.3 μm (in air). In order to introduce the pump into the Zeiss stereo-microscope (Discovery,V8) system a dichroic mirror (Thorlabs, DMSP650L) was placed just ahead of the microscope objective. The dichroic was highly reflective at 663 nm but gave -2 dB loss at 1310 nm. Nevetheless, the view through the eyepieces of the Zeiss stereo microscope was good enough to align the sample in the imaging systems field of view.

The OCT line rate was 10 KHz using our FD-OCT (300 M-scans) and 100 KHz using our SS-OCT system (10,000 M-scans). Molecular contrast OCT images with the MB-PLGA particles were processed in the following way. The pump laser was amplitude modulated at frequency f, while collecting an OCT M-scan. The M-scan was processed normally to get the complex OCT signal as a function of time. A Fourier transform of the signal along the time dimension was calculated. The frequency domain signal was then filtered around the pump frequency, f. The only difference between PPOCT and PTOCT processing was that for PPOCT the magnitude of the OCT M-scan is analyzed in the frequency domain while for PTOCT the phase of the OCT M-scan is analyzed. One M-scan leads to one A-line in the molecular contrast image.

An in vitro setup was used to test and characterize the signal generated from the MB-based contrast agents. PLGA microparticles with MB concentrations of 8.9, 22.9 and 42.9 mM were suspended in DPBS and loaded into 200 μm inner diameter capillary tubes. Tubes were imaged using the FD-OCT system with a pump power of 4.4 mW and probe power of 3.5 mW. A contrast-to-noise-ratio (CNR) was defined as the ratio of the signal magnitude at the modulation frequency divided by the noise floor. The noise floor was defined as the median of the magnitude at frequency bands at ±1 kHz relative to the pump modulation frequency [5]. A ratio of 4 was experimentally determined as an acceptable pump-probe signal detection threshold that effectively removed all background. Similarly, soluble MB, MB microparticles and MB nanoparticles were suspended in DPBS, and transferred into 500 μm diameter PDMS microchannels. The backscattering and the molecular contrast signal generated from the MB solutions and PLGA particles were evaluated by imaging with both the FD-OCT and SS-OCT systems.

Biomedical Optics EXPRESS

Coronary segments from human hearts were harvested from non-specific adult autopsy cases according to a protocol approved by the Texas A&M University Institutional Review Board. The artery sections were immediately stored in DPBS at 4°C and used within 48 hours. Arterial segments were cut along the longitudinal direction of the vessel, hydrated with warm DPBS (37°C) and placed inside a custom-made parallel flow chamber with the lumen facing up. Tissues were treated with either MB solution (50 μg/mL), a-VCAM1 functionalized MB-PLGA microparticles (1×10^7 p/mL) and MB nanoparticles (1.84×10^{10} p/mL) suspended in DPBS, and incubated at 37°C for 20 minutes. Arterial segments incubated with DPBS solution and non-targeted MB-PLGA particles were used as a control. After incubation, arteries were washed with DPBS (37°C) under laminar flow (wall shear rate = 100 s^{-1}) for 5 minutes to remove unbounded particles and imaged using the previously described FD-OCT system. After imaging, the arterial segments were fixed in formalin and sent to a histology lab to get tissue slides prepared. India ink was used to label the arterial cross sections scanned with our FD-OCT. Evaluation of digitized artery segments was performed to evaluate particle binding and endothelium permeability of MB PLGA particles.

3. Results

3.1. Nano-/microparticle synthesis and characterization

Methylene blue loaded PLGA particles were prepared by a modified single oil-in-water (O/W) emulsion solvent evaporation method. By controlling the shear stress applied during the emulsification process, PLGA microparticles and nanoparticles were successfully synthesized with an average diameter of 2.7 μm (± 1 μm) and 84 nm (± 30 nm), respectively. These two particle sizes are chosen based on our previous studies and others, which demonstrates that 2-3 μm is an optimal particle size for targeting the vascular wall in atherosclerotic-flow conditions while < 200 nm nanoparticles are suitable for penetrating into a deeper tissue layers [25,32–34]. Overall, using our modified O/W emulsion solvent evaporation methods, MB-PLGA particles were produced at a rate of 1.44×10^8 microparticles/hour or 4.22×10^{12} nanoparticles/hour. They are spherical in shape with fairly smooth surfaces [Figs. 1(A) and 1(C)] and have an average MB encapsulation efficiency of 82.6% in microspheres and 48.4% in nanospheres. Physicochemical properties of MB-PLGA particles were determined by measuring their absorption spectra via spectrometry. MB is a cationic phenothiazine dye with an absorption peak at 664 nm in its monomeric form. At high concentration (> 20 μM) or upon interaction with oppositely charged surface, MB tends to aggregate and form dimers [35,36], which exhibit a distinct absorption peak at ~ 600 nm [see Fig. 2(A)]. Figure 3(A) shows the optical density of free MB (30 μM), MB-PLGA microparticles and MB-PLGA nanoparticles in DI water. All MB formulations exhibit similar spectra. The long tail at shorter wavelengths on the MB nanoparticles spectrum is mainly due to particle-size dependent light scattering. The presence of a primary absorption peak at 664 nm and a secondary peak at 600 nm, indicates the formation of both MB monomers and dimers in all cases. The extent of MB dimerization, however, is different and can be evaluated by calculating the ratio of absorbance at 600 to 664 nm, namely a dimer to monomer ratio (D/M). Free MB (30 μM) had the D/M ratio of 0.61. As free MB concentration in solution increases from 20 μM to 200 μM, the D/M ratio increases from 0.59 to 1 [Fig. 2(A)], as expected [37]. However, further decrease of MB concentration below 20 μM, does not affect the D/M ratio. Instead, higher MB concentration is favorable in this concentration range because it provides stronger absorbance.

At equivalent total MB mass, MB embedded in PLGA particles demonstrated higher D/M ratios relative to that of free MB, i.e. 0.87 in microparticles and 0.95 in nanoparticles compared to 0.61 in free MB [Fig. 3(A)]. This is likely because encapsulation increases local MB concentration, which seems to induce MB aggregation within the particles. In addition, negatively charged COOH-PLGA polymer used in this study possibly further enhances MB aggregation as it can

Biomedical Optics EXPRESS

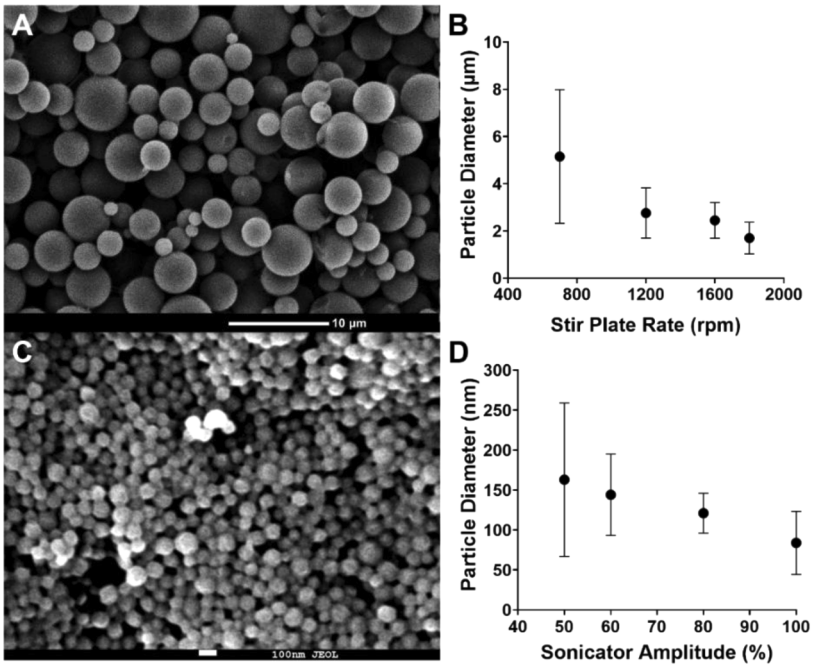

Fig. 1. SEM images of (**A**) MB-PLGA microparticles (50:50 PLGA) and (**C**) MB-PLGA nanoparticles (75:25 PLGA). Effect of mechanical stir speed on MB-PLGA particle size: (**B**) Magnetic stirrer speed on 50:50 PLGA microparticles (3% surfactant, pH 8.4), (**D**) Sonicator tip resonance amplitude on 75:25 PLGA nanoparticles (3% surfactant, pH 8.4). Value = mean ± SD (n = 3, number of particle batches analyzed).

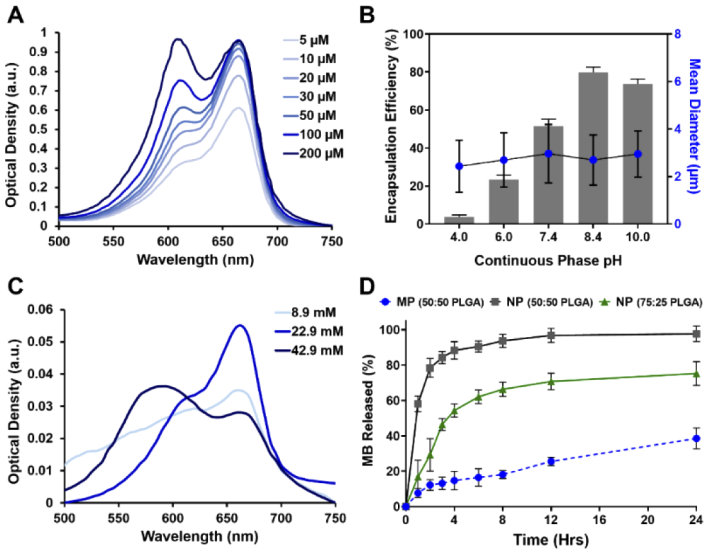

Fig. 2. (**A**) Optical density of methylene blue solutions at different concentrations suspended in DI water. (**B**) Effect of continuous phase pH on MB encapsulation efficiency and particle size of PLGA microparticles (50:50 PLGA, 3% surfactant). (**C**) Optical density spectrum of PLGA microparticles loaded with different concentrations of methylene blue. (**D**) Methylene blue release from 50:50 PLGA microparticles and 50:50 and 75:25 PLGA nanoparticles in DPBS at pH 7.4, 37°C. Value = mean ± SD (n = 3).

Biomedical Optics EXPRESS

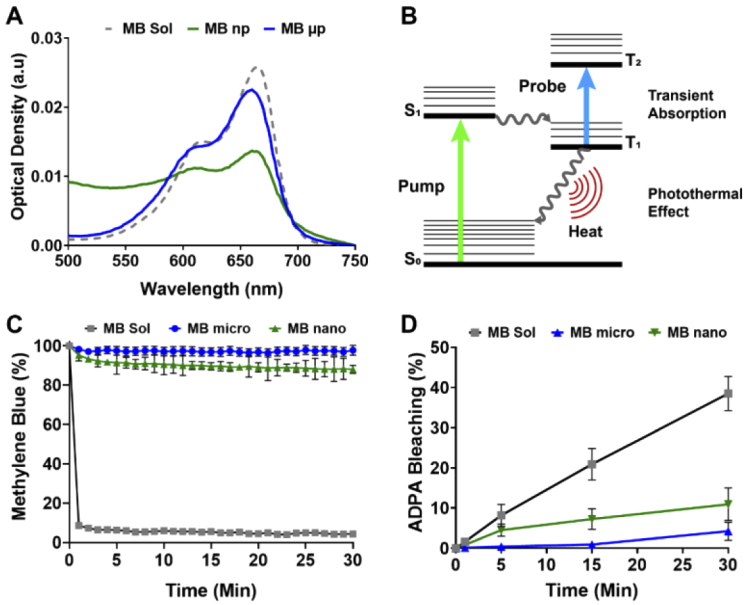

Fig. 3. **(A)** Normalized absorption spectrum of MB solution, MB-PLGA microparticles (MB µp), and nanoparticles (MB np). **(B)** Diagram of molecular energy transitions for the methylene blue transient absorption and photothermal effect. Driven energy transitions are indicated by straight arrows and spontaneous transitions as wavy arrows. **(C)** Normalized MB fluorescence emission at 680 nm over time after addition of NADH enzyme to free MB, MB-PLGA microparticles and MB-PLGA nanoparticles in DI water. **(D)** Percentage of ADPA bleaching for free MB, MB-PLGA microparticles and MB-PLGA-nanoparticles with our pump 660 nm light source for 30 min. Value = mean ± SD (n = 3).

attract MB (positively charge in solution) binding to the surface [18,36,38]. Since the efficiency of both PPOCT and PTOCT techniques partially depends on the absorbance intensity of MB at the pump wavelength (663 nm), MB contrast agent formulation can be optimized such that the MB monomeric form is maximal. For instance, an internal concentration of 22.9 mM MB in PLGA particles is optimal as an OCT contrast agent (Fig. 7). As we have shown previously for PPOCT [39], we expect the CNR to grow with concentration, peak, and get smaller as the concentration continues to grow.

The emulsion solvent evaporation method has been widely used to fabricate various polymeric particles [16,40]. Along with the mechanism of particle formation, several fabrication process parameters such as emulsification speed, surfactant concentration, polymer ratio, and viscosity and pH of the continuous phase, have been extensively investigated [41–43]. Similar to others, our study showed that the mechanical stir speed during the emulsification process dominantly control particle size. As the mechanical stir speed increases from 700 rpm to 1800 rpm, particle size decreases from 5.15 µm to 1.70 µm [Fig. 1(B)]. The higher shear force generated by the increase in the stir speed causes the emulsified droplets to break up and yield smaller particles. Further increase in shear energy generated by a sonicator could reduce particle size down to 84 nm [Fig. 1(D)].

In addition to the stir speed, pH of the continuous aqueous phase significantly affects MB-PLGA particle formation and MB encapsulation efficiency. Since MB is a hydrophilic molecule, MB favorably partitioned out of the organic phase to the aqueous continuous phase during the emulsification and solvent evaporation process, resulting in relatively low MB encapsulation efficiency at neutral pH [44]. As pH increased from 6 to 10, encapsulation efficiency increased

Biomedical Optics EXPRESS

from 26% to 83% [Fig. 2(B)]. This is partly because the level of MB dimerization increases with the continuous phase pH [45]. The formation of MB dimers and MB aggregates in alkaline solution may delay and hinder MB molecules from leaking out of the polymer matrix during the fabrication process. Further increase to pH 10 resulted in decrease of encapsulation efficiency while no significant difference in particle recovery was observed between pH of 8 and 10. As shown in Fig. 2(B), the particle size was not affected by the change of the continuous phase pH. By using a water phase pH of 8.4, MB was encapsulated intro micro particles with an encapsulation efficiency of 82.6%. Similarly, PLGA nanoparticles were fabricated with a MB encapsulation efficiency of 48.4%.

Cumulative release of MB from PLGA micro and nanoparticles were studied in DPBS at pH 7.4, 37° C for 24 hours. Considering the average procedural and imaging times of OCT we chose to evaluate the MB release at two hours, expecting that would be sufficient for most imaging protocols. MB release during this time window must be controlled to maintain sufficient MB signal throughout the process. As shown in Fig. 2(D), MB-PLGA (50:50) microparticles demonstrated a sustained release profile with ~11% of total MB release in 2 hours. On the other hand, MB-PLGA (50:50) nanoparticles displayed a burst release profile with ~ 81% of MB release in 2 hours [Fig. 2(D)]. The significant higher release rate from nanoparticles compared to microparticles is likely due to an increase in surface-to-volume ratio as particles become smaller. To reduce the amount of MB release, MB-PLGA nanoparticles were fabricated using 75:25 PLGA polymer with the same base formulations. Figure 2(D) shows that the MB release from 75:25 PLGA nanoparticles was significantly reduced particularly in the first few hours, i.e. 46% of total MB at the 2-hour window. This result agrees with previous work reporting that a slower release profile is associated with a PLGA polymer having a higher lactic acid to glycolic acid ratio [41,46]. The efficiency of MB as a contrast agent in biological environment is in part inhibited by its lack of target specificity and relatively short circulation lifetime. An average of 78% of MB is reduced by NADH/NADPH dehydrogenases and/or enzyme reductase in red blood cells and peripheral cells to colorless leucomethylene blue (LMB) [7,47,48]. The photophysics of LMB are substantially different than MB rendering it invisible to our imaging system. Microencapsulation has been previously used to protect MB from the enzymatic reduction [20].

In order to demonstrate that our formulation also provides protection from reduction to LMB we did the following experiment. To mimic the enzyme activities in the biological environment, free MB and MB-PLGA particles in DI water were sequentially incubated with NADH and diaphorase (NADH dehydrogenase). The fluorescence intensity of MB at 680 nm was monitored for an hour. The decrease in fluorescence intensity indicates the reduction of MB into LMB, which lacks emission at this wavelength. As shown in Fig. 3(C), approximately

96% of free MB was rapidly reduced within the first two minutes. In contrast, by encapsulating MB within PLGA particles, only 5% of MB in microparticles and 12% of MB in nanoparticles was reduced. These results indicate that a majority of MB remains sequestered within the PLGA matrix and therefore protected from enzymatic reduction.

MB has been investigated as a therapeutic agent, particularly in photodynamic therapy (PDT), because of its high yield of singlet oxygen ($^1O_2$) generation, and membrane permeability [49,50]. In PDT, relaxation of excited MB molecules into the ground state generate reactive oxygen species (ROS), which irreversibly causes damage to nearby cells. Although the $^1O_2$ generation is favorable in PDT for cancer treatment, it is an undesirable side effect for a contrast agent, hence we sought to minimize ROS production.

Microencapsulation is a potential approach to regulate $^1O_2$ local release by controlling the polymeric network and the sequestration of MB molecules within particle shells [20,51,52]. In this study, MB was entrapped within the PLGA polymeric matrix non-covalently. Our hypothesis is that MB-PLGA could potentially reduce, or at least delay, the local release of $^1O_2$ to their surrounding environment. To test this hypothesis, free MB, MB-PLGA microparticles and

Biomedical Optics EXPRESS

MB-PLGA nanoparticles were illuminated with the pump light source at 660 nm for up to 30 min. The release of $^1O_2$ from irradiated MB to aqueous solution was monitored using a chemical probe, ADPA [20,52]. Once ADPA reacts with $^1O_2$, it is irreversibly reduced into ADPA endoperoxide, which causes a decrease in the fluorescence emission of ADPA at 400 nm. The decrease in ADPA fluorescent intensity, reported as the percentage of ADPA bleaching in Fig. 3(D), indirectly estimates the efficiency of $^1O_2$ generation and release into the surrounding environment. As previously shown in existing studies, free MB generates $^1O_2$ upon irradiation while exhibiting no cytotoxicity without illumination (i.e. low dark toxicity) [20,22,53]. In contrast, MB embedded within PLGA microparticles and nanoparticles favorably reduced the release of $^1O_2$ by 97% (34-fold) and 75% (4-fold) relative to that of free MB, respectively. This reduction is likely due to a delayed diffusion of $^1O_2$ through the polymer network to the outside where they can interact with the ADPA molecules. These results show that MB-PLGA particles can reduce local release of $^1O_2$ thus mitigating the unwanted associated cell death.

To enable active targeting on the inflamed vascular wall, we functionalized biotin-VCAM-1 antibodies on MB-PLGA micro and nanospheres surface [Fig. 4(A)]. Microparticles functionalization was confirmed by flow cytometry using FITC-secondary antibodies [Fig. 4(B)]. Human aVCAM-1 ligands were immobilized on MB microparticles with a site density of approximate 2959.7 sites/μm^2. Functionalization of PLGA-MB nanoparticles was estimated by an ELISA assay. The fluorescence intensity generated by the secondary antibody attached to both micro and nanoparticles suggest a 2-fold increase of site density on nanospheres compared to microspheres [Fig. 4(C)]. This result was expected for nanoparticles due to their higher ratio of surface area per particle volume allowing them to capture more ligands.

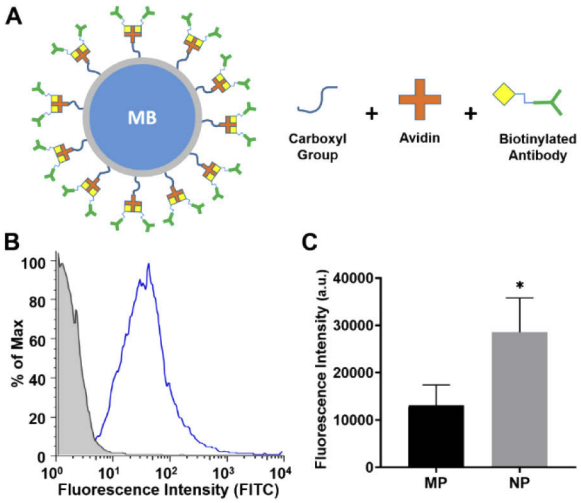

Fig. 4. **(A)** Schematic of PLGA particle surface functionalization with biotinylated antibodies. **(B)** Flow cytometry histogram of aVCAM-1 MB-PLGA microparticles labeled with a FITC-secondary antibody (blue) and uncoated MB-PLGA microparticles (gray). **(C)** ELISA assay results of functionalized MB-PLGA micro (MP) and nanoparticles (NP) (HRP-secondary antibody). Statistical significance is indicated as * for $p < 0.05$.

3.2. *Molecular Contrast Imaging*

As an OCT contrast agent, MB enables two molecular contrast pathways: transient absorption and photothermal effect [Fig. 3(B)]. MB molecules irradiated with a pump light source (peak at 660 nm), reach the singlet excited state and rapidly populate the ground triplet state through

Biomedical Optics EXPRESS

intersystem crossing. Once in the ground triplet state, MB molecules can further absorb probe light (peak at 830 nm) or return to the singlet ground state through non-radiative relaxation (vibrational, collisional, etc.).

Fourier analysis of FD-OCT M-scans reveals clear contrast encoded in both the magnitude and the phase components of the OCT signal at the pump modulation frequency (Fig. 5). Pump-probe spectroscopy analysis revealed a bi-exponential decay for MB molecules encapsulated into PLGA spheres, potentially an indicator for signal contribution from both transient absorption and photothermal effect [Fig. 6.(A)]. MB-PLGA particles decay was calculated to have an average lifetime of 394.7 µs. Longer triplet state lifetimes were observed when the particle solution was bubbled with N_2 to remove dissolved oxygen [(Figs. 6(C) and 6(D)]. MB solution presented a mono-exponential decay with an average lifetime of around 2.2 µs [Fig. 6(B)], in agreement with previously reported values [37].

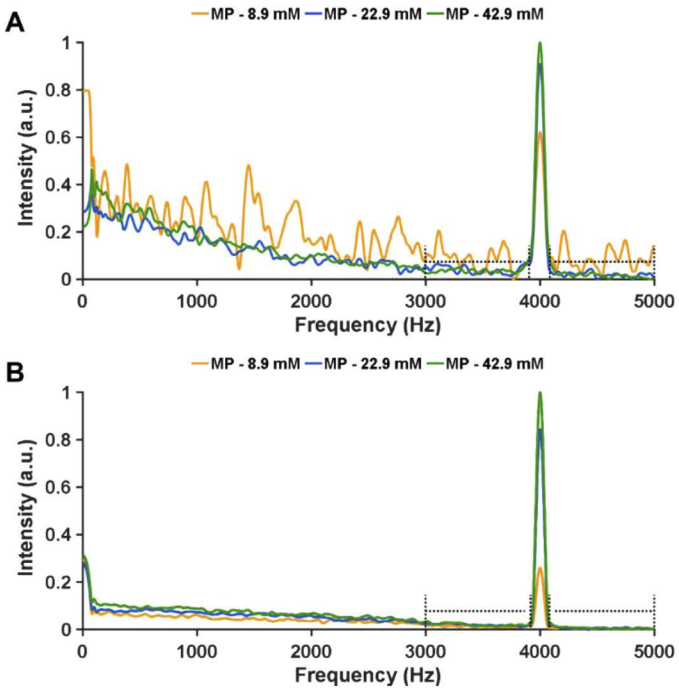

Fig. 5. Fourier domain analysis along time of (A) magnitude and (B) phase components from FD-OCT M-scans containing signal MB microparticles. Doted lines indicate range of frequencies considered as noise floor.

MB microparticles were loaded into capillary tubes (200 µm inner diameter), imaged with our FD-OCT system and their CNRs were estimated from the processed OCT B-Scans. PLGA microparticles loaded with 8.9, 22.9 and 42.9 mM MB, had CNRs of 4.43, 5.47 and 5.86, respectively [Fig. 7(E)]. Similar CNR trends were observed for nanoparticles. Based on CNR results, PLGA microspheres loaded with 22.9 mM MB and nanoparticles loaded with 20.6 mM MB were considered good candidates for OCT contrast agents.

Biomedical Optics EXPRESS

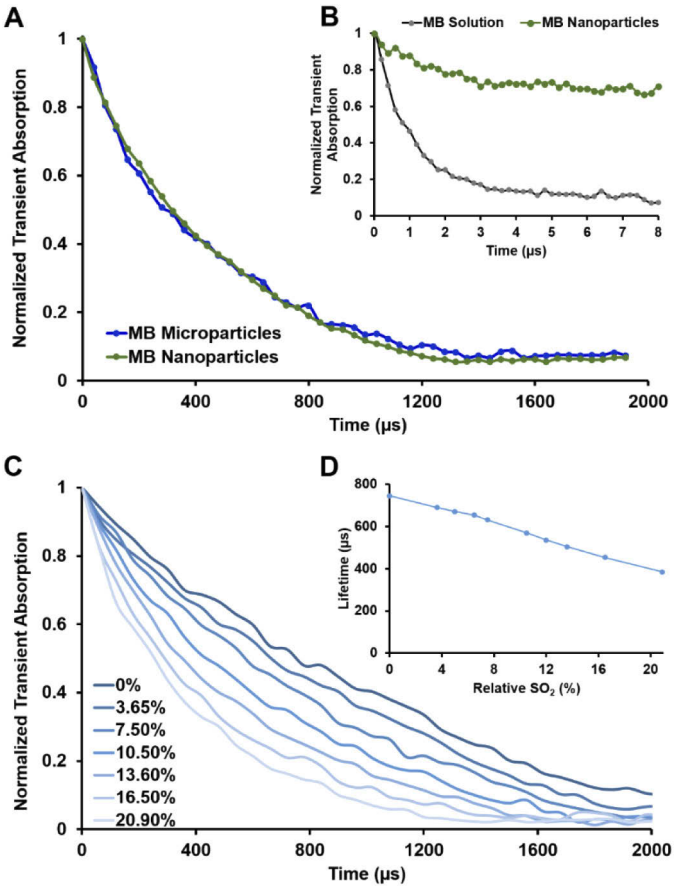

Fig. 6. Transient absorption decays of **(A)** MB-PLGA micro and nanoparticles, and **(B)** MB solution and MB nanoparticles suspended in DI water with atmospheric oxygen saturation (assumed a SO_2 of 20.95%). **(C)** Transient absorption decays of MB-PLGA nanoparticles at different relative SO_2%. **(B)** Avg lifetime of MB nanoparticles as function of relative SO_2%. NEOFOX oxygen sensor probe (Ocean Optics, Inc.) was used to estimate the relative SO_2%.

Biomedical Optics EXPRESS

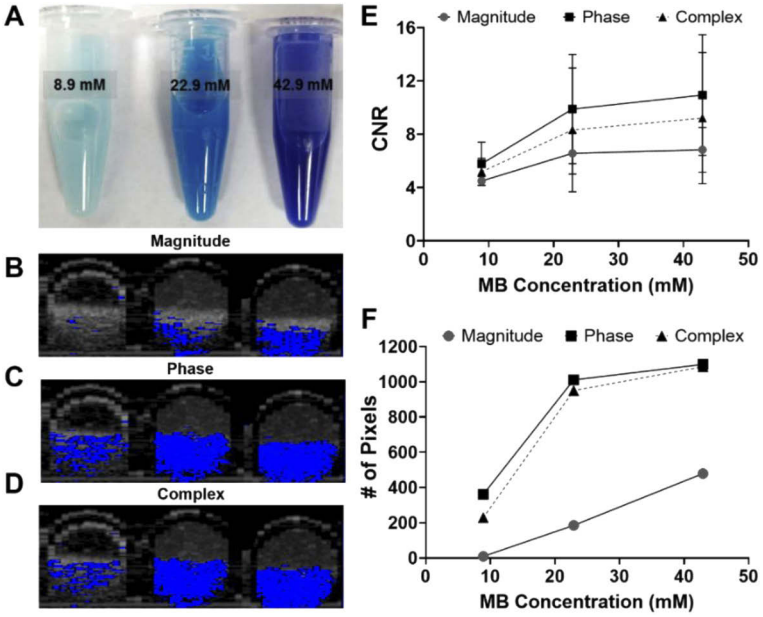

Fig. 7. **(A)** PLGA microparticles with average diameter of 2.7 µm loaded with 8.9, 22.9 and 42.9 mM of MB. **(B)** Magnitude and **(C)** phase and (**D**) complex B-scans of MB-PLGA particles suspended in 200 µm capillary tubes. **(E)** CNR values at the magnitude, phase and complex images for each batch of PLGA-MB microparticles. (**F**) Number of pixels with CNR greater than the established threshold (CNR≥4).

In order to compare the molecular contrast OCT signal generated from MB solution, microparticles and nanoparticles, suspensions were prepared in DPBS and introduced into PDMS microchannels (500 µm diameter). MB molecules in solution or encapsulated were irradiated by the modulated pump light source enabling contrast. The signals at the pump modulation frequency (4 kHz) due to the contrast agent are displayed in Fig. 8. The OCT B-scan is shown in gray scale, with the molecular contrast signal shown in a blue scale overlay. The first column is with no pump light, hence we expect no molecular contrast signal. Indeed, the signal at the modulation frequency was below the established threshold (for the magnitude, phase, and complex signals). The following 3 columns represent the magnitude of a temporal (time-dimension of M-scan) Fourier transform at the pump modulation frequency. The FFT was calculated for the interferometric magnitude, phase or complex (magnitude and phase) signals. From our prior experience [27], we expected signal due to transient absorption to be primarily in the magnitude (column 2), photothermal in the phase (column 3), with the complex incorporating both mechanisms for molecular contrast. This data is consistent with that expectation. The FD-OCT system which can measure signal from both transient absorption and photothermal effects shows signal in both the magnitude and phase. However, the SS-OCT which should be insensitive to transient absorption only shows signal in the phase. In other words, the system with a probe at the triplet state absorption frequency (830 nm) shows signal from both transient absorption and photothermal effects while the system with a non-resonant probe (1310 nm) only shows signal due to the photothermal effect.

To further study the feasibility of MB-PLGA particles as targeted molecular contrast agents for OCT, we designed an ex-vivo experiment to validate binding of aVCAM-1 functionalized MB-PLGA particles. Artery segments were processed as outlined in methods. Artery sections treated with MB solution (50 µg/mL) or non-targeted MB-PLGA particles did not show OCT contrast (images not shown). The lack of contrast signal was expected as a result of the washing

Biomedical Optics EXPRESS

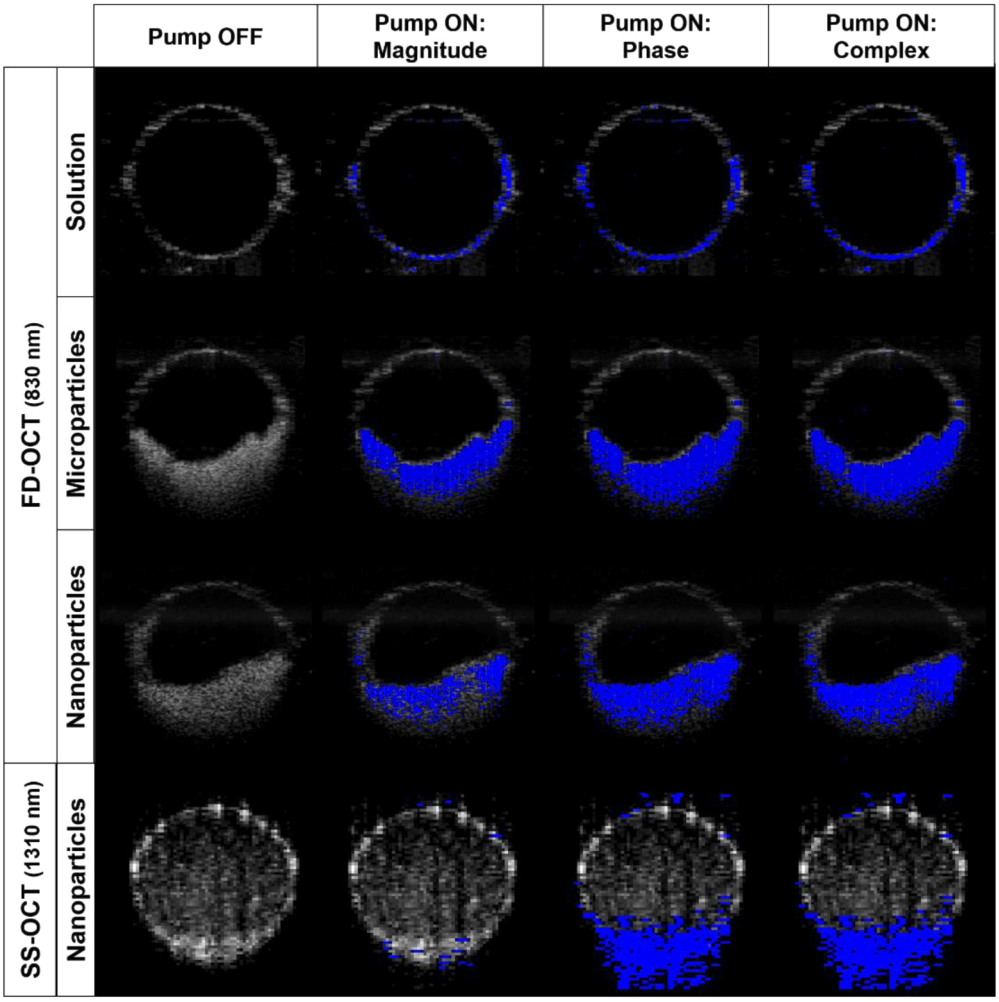

Fig. 8. PDMS microchannels (500 µm inner diameter) loaded with MB solution, MB-PLGA microparticles and MB-PLGA nanoparticles. The OCT B-scan is shown in gray scale with the molecular contrast signal overlain in blue. Images were recorded with the FD-OCT system (830 nm probe) for the top 3 rows and the SS-OCT system (1310 nm) in the bottom row. Note: The nanospheres had not entirely settled to the bottom of the microchannel in the SS-OCT images, hence the weak signal above a stronger signal at the bottom of the microchannel. Pump-off images show no molecular contrast signal because the threshold, CNR≥4, was sufficient to remove all background, hence there was no molecular contrast signal when the pump was off.

Biomedical Optics EXPRESS

step with DPBS solution which likely washed away the MB solution and removed the unbounded particles. Resulting images for both targeted micro and nanoparticles are shown in Fig. 9. As expected, the MB microspheres (3.7 μm) mostly remained near the surface [Fig. 9(A)] while the nanospheres (84 nm) penetrated more deeply [Fig. 9(C)].

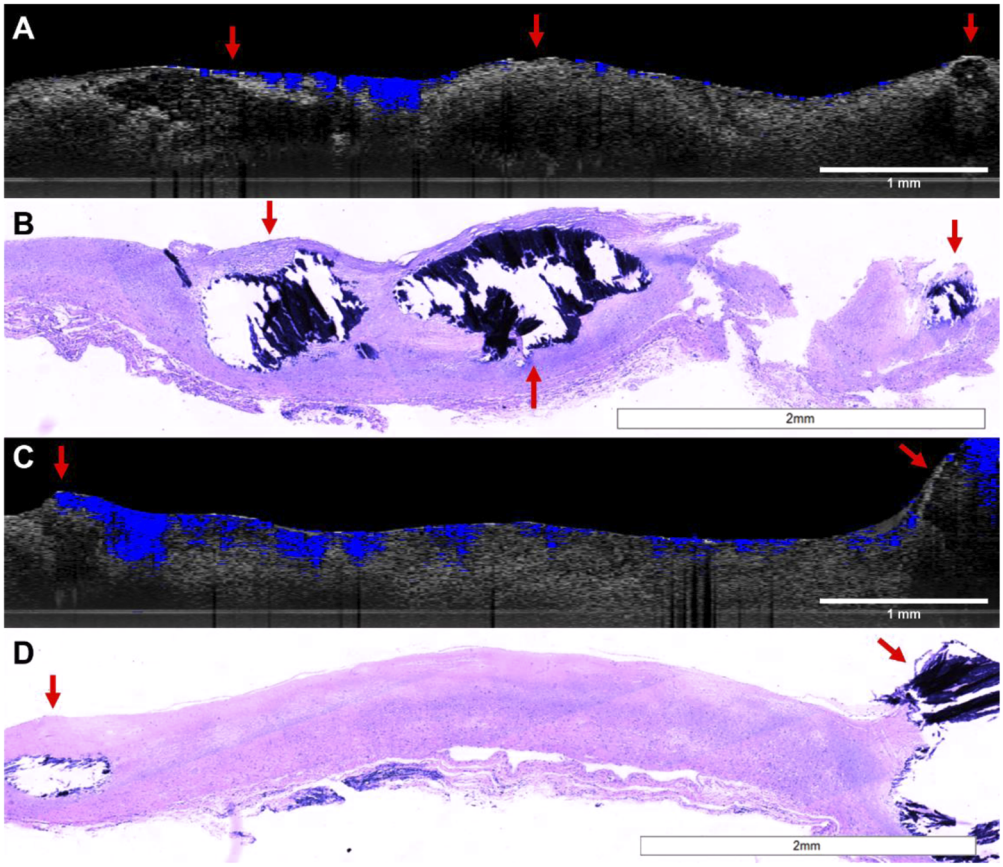

Fig. 9. Images of human artery sections treated with **(A-B)** aVCAM-1 MB-PLGA microparticles and **(C-D)** aVCAM-1 MB-PLGA nanoparticles. OCT B-scans (gray scale) with overlain molecular contrast (complex) signal (blue) (A,C) and their respective histology sections (B,D). Calcified regions are indicated with reds arrows.

4. Discussion

Despite high spatial resolution, OCT typically only provides morphological information of biological tissues. Since OCT contrast mainly relies on variations of tissue refractive index, most endogenous molecular biomarkers do not produce unique OCT signals. Several exogenous OCT contrast agents such as indocyanine green dye (ICG) [54], gold nanoparticles [55], intralipid fat emulsion [56,57], and Janus microspheres [58], have been introduced to provide molecular information. However, most of these approaches have experienced limited success due to lack of target specificity, high concentrations needed to be detected, and poor biodegradability/clearance.

Here we have explored biodegradable PLGA-based contrast agents for molecular imaging with OCT, nominally for targeting atherosclerotic lesions. PLGA-based carriers have been broadly used as contrast agents and therapeutics in the clinic due to their safety and relatively simple fabrication [54]. The contrast agents were designed to enhance morphological image contrast and

Biomedical Optics EXPRESS

provide molecular details at the arterial surface and within the atherosclerotic plaque, which could prove important for predicting plaque vulnerability. Since the efficiency of particle localization on and within tissues has been shown to be size-dependent [25,26], e.g. microparticles favor vascular surface targeting while nanoparticles favor intracellular penetration, the PLGA-based contrasts agents were fabricated into two size ranges (2.7 μm, 84 nm) (Fig. 1) to optimally target both locations.

Methylene blue was selected as our contrast agent due to its low cytotoxicity, its ground and triplet state absorption peaks that match available light sources and its clinical use. The functionality of methylene blue as an OCT contrast agent is impacted by the co-presence of MB in monomeric and dimeric forms. Generally, as the concentration of MB in free solution increases (from 20 μM to 200 μM), the D/M ratio increases [Fig. 2(A)]. Similar results were also observed when MB was encapsulated within PLGA microparticles [Fig. 2(C)].

Our experiments have shown that the encapsulation efficiency can be modulated by the pH of water phase used during the emulsification process. As the water phase pH increases, the encapsulation efficiency was found to increase linearly from pH 4 to pH 8.4 [Fig. 2(B)]. This could be partly because the level of MB dimerization was enhanced in the alkaline solution [45,59]. The formation of MB aggregates may delay and hinder MB molecule clusters from leaking out of the polymer matrix/shell during the fabrication process, resulting in the higher encapsulation efficiency at a higher pH. In addition, it is possible that the increase of water phase pH changes the charge distribution/polarity at the water phase-PLGA chain border, which slows down the MB diffusion to the outer phase [60,61]. Microparticles synthesized using a pH of 8.4, provided the best encapsulation efficiency (82.6%). As shown on Fig. 7(E), the improvement in CNR was relatively small at nearly double the MB concentration (from 22.9 mM to 42.9 mM). Therefore, 22.9 mM was chosen as a good compromise between signal strength and MB dosage. Once the optimal fabrication parameters were determined for microparticles, MB-PLGA nanospheres were prepared following the same protocol with the only difference being the shear stress/time applied to the emulsion.

PLGA particles are biodegradable and thus expected to release drugs in physiological conditions over time. Monomer ratio (lactic acid:glycolic acid) and polymer molecular weights are common PLGA properties that are varied to achieve desired drug release kinetics and profiles for specific applications. As shown in Fig. 2(D), 50:50 PLGA nanoparticles loaded with 20.6 mM released 81% of encapsulated MB in the first 2 hours of incubation at 37 °C, compared to 11% of MB from 50:50 PLGA microparticles during the same time frame. The faster release profiles from nanospheres could be explained by a greater surface-to-volume ratio compared to microparticles and the overall positioning of MB molecules concentrated relatively close to the sphere surface. By fabricating the nanoparticles using PLGA having a higher molecular weight and a higher lactic/glycolic ratio (75:25), the MB release was shown to be significantly reduced particularly during the first 2 hours. This result agrees with previous works reporting that a slower release profile is associated with PLGA polymer with a higher lactic acid to glycolic acid ratio [41,46]. Although some of MB might be released during in-vivo imaging procedures, our in-vitro studies [Fig. 2(D)] suggest that the MB release from 50:50 PLGA microspheres and 75:25 PLGA nanospheres during this time window should not compromise the contrast imaging sensitivity.

The PLGA carrier system provides an environment where the physical distribution and the state of MB molecules are preserved, unlike free MB. The susceptibility of enzymatic reduction is one of methylene blue's biggest drawbacks for in-vivo therapeutic and molecular imaging applications. In circulation, MB is reduced by either NADH/NADPH dehydrogenases or enzyme reductase in red blood cells and peripheral cells to colorless leucomethylene blue (LMB) [24–26], rendering it invisible to our molecular contrast OCT imaging system. By encapsulating MB into PLGA particles, MB was protected from the enzymatic interaction. Specifically, 95% of MB encapsulated within microparticles and 88% of MB encapsulated within nanoparticles remained

Biomedical Optics EXPRESS

in their native states after 30 min of enzymatic exposure [Fig. 3(C)]. These results indicate that a majority of MB remains immobilized within the PLGA matrix during the treatment. The slight decrease of MB intensity could be attributed to the reduction of MB molecules bound at the particle surface. This result demonstrates that a protective environment formed by the PLGA matrix successfully prevents large enzymatic molecules to penetrate and interact with the encapsulated MB. Thus, MB-PLGA provides extended photostability of MB in circulation, which in turn reduces the need of high doses and potentially minimizes associated cytotoxicity. These results suggest that encapsulation of MB into PLGA could be beneficial for other clinical applications such as sentinel lymph node detection.

Upon 660 nm excitation, MB molecules generate reactive species which can deconstruct and compromise the integrity of proximal tissues. This property has been investigated extensively in the context of photodynamic therapy, but is undesirable in diagnostic applications. Figure 3(D) shows that the local generation of radical species by excited MB was significantly reduced when MB was encapsulated within PLGA particles. This reduction could be contributed to several factors including the formation of MB dimers [Fig. 3(A)], a longer diffusion path within the PLGA matrix [51], and a quenching of MB excited states. Since MB dimers have a different absorption peak (at 600 nm, compared to 660 nm for MB monomers), they do not produce $^1O_2$ upon 660 nm irradiation. Also, there are two photochemical pathways (type I and type II) that are involved in the photoinduced generation of reactive species [35,38]. In type I mechanism, excited MB transfers electrons to biomolecules and forms several different radical species. In type II, excited MB transfers energy to surrounding oxygen molecules and generates $^1O_2$. Type II is generally accepted as a primary pathway that is responsible for photobiological activities while type I is a secondary mechanism [62]. MB dimers have been previously shown to shift the photochemical pathways for MB from type II to type I, resulting in the decrease in $^1O_2$ formation [36,38]. Lastly, since $^1O_2$ molecules exist just for a few microseconds, a longer diffusion time could mean that $^1O_2$ generated by MB inside of the sphere recovers to the stable form, $^3O_2$, before exiting the particle. This result shows that MB-PLGA particles can hinder $^1O_2$ production external to the particle, thus mitigating associated adverse effects. Although, MB dimers seem to prevent the generation of $^1O_2$, they don't contribute to the generation of Pump-Probe contrast. Therefore, a low D/M ratio is still preferred inside the PLGA particles.

In the context of the results noted above, we would argue that MB-PLGA is a superior contrast agent over free MB. The PLGA matrix provides protection against leuco-MB production and unwanted photoinduced generation of reactive species. As a contrast agent for OCT it provides high local concentration as well as a much higher scattering cross-section than free MB. The latter is clearly demonstrated in Fig. 8 (top row) where the molecular contrast signal is only registered at the walls of the tube because there is no detectable scattering in the aqueous solution of MB. Compare that to the lower three rows where the PLGA particles provide strong scattering contrast. This provides for better localization of the molecular contrast signal.

The imaged ex vivo human arterial segments corresponded to fibrocalcific plaques as observed in the OCT B-scans [Figs. 9(A) and (C)] and confirmed by histopathology [Figs. 9(B) and (D))]. The OCT B-scan in Fig. 9(A) shows highly attenuated areas with fairly well-defined boundaries in the center and right end of the segment. The accumulation of aVCAM-1 MB-PLGA microparticles is confined to the low-attenuated fibrotic tissue surrounding the calcified areas. As expected, the acellular calcified areas do not show microparticle accumulation. The histology in Fig. 9(B) clearly confirms the presence of large calcified areas in the center of the segment shown as void areas with dark blue fragmented calcification debris (a small calcified area is also seen on the right end of the segment). The OCT B-scan in Fig. 9(C) shows low-attenuated fibrotic areas in the center of the segment, and small highly attenuated areas with fairly well-defined boundaries at both ends of the tissue sections. Accumulation of aVCAM-1 MB-PLGA nanoparticles was observed throughout the fibrotic plaque areas and around the calcifications. The histology section

Biomedical Optics EXPRESS

shown on Fig. 9(D) clearly confirms a mostly fibrotic plaque with calcified areas on both ends. These results suggest that targeted MB-PLGA micro and nanoparticles were mainly accumulated in fibrotic regions of the arterial sections.

Although vascular endothelial integrity could be compromised in ex-vivo tissues, our ex-vivo experiments presented a similar particle permeability trend to findings observed from in-vivo experiments performed elsewhere [33,63]. Since the ex-vivo experiment was performed under static incubation, penetration of PLGA particles through the arterial endothelium was mainly determined by sphere average diameter (Fig. 9). Endothelial cell junction gaps in atherosclerotic plaques might be big enough to allow nanoparticles to permeate much deeper than microspheres, making them a better approach for foam cells targeting and imaging [33,34]. Higher permeability of MB nanoparticles under in-vivo pressure and flow conditions could be expected, making these contrast potentially useful for imaging and characterization of plaque biomarkers in deeper tissue layers.

For simplicity, only one cell adhesion molecule (VCAM-1) was used to conjugate MB micro and nanoparticles. However, the methodology presented can be used to functionalize PLGA spheres with other biotinylated molecules/antibodies to target/image other critical biomarkers in atherosclerosis such as CD36, a membrane protein related to macrophage foam cell formation. These targeted PLGA platforms could therefore enable the characterization of pathogenic processes by investigating molecular activity and receptor expression at the vascular endothelium. Ex-vivo experiments confirmed binding of functionalized MB-PLGA particles to human vascular endothelium inflammatory receptors. A static incubation of aVCAM-1 micro and nanoparticles was selected due to the dimensions of the custom-made flow chamber, since a large number of spheres would have been needed to run a flow experiment at the rate and particle concentration desired. To minimize the effect of non-specific binding of PLGA particles, artery sections were washed under flow at 100 s^{-1} with DPBS+. Molecular contrast OCT images demonstrates the potential of these targeted contrast agents. Although MB and PLGA polymers have been safely used on several medical applications [2,38,64], other factors such as particle circulation time, vascular margination and targeting efficiency must be studied and optimized to before the in vivo translation of these contrast agents.

5. Conclusions

In conclusion, we have developed a versatile robust molecular contrast agent by combining the advantages of a biodegradable polymer and the spectral properties of methylene blue that can provide specific labeling of biomarkers in atherosclerosis and other diseases. PLGA particles loaded with MB, were fabricated into spheres with average diameters of 2.7 μm and 84 nm and encapsulation efficiencies above 48%. The enhancement of chemical and photo-stability of encapsulated MB was experimentally confirmed. To the best of our knowledge, this is the first time that MB loaded PLGA particles are used as molecular contrast agents for OCT.

Funding

National Institutes of Health (R01HL111361); American Heart Association (17SDG33660894); Consejo Nacional de Ciencia y Tecnología (514628).

Acknowledgments

We gratefully acknowledge Dr. Jessie Adame MD (Autopsy and Pathology Services) for providing postmortem human coronary segments.

Disclosures

The authors declare no conflicts of interest.

Biomedical Optics EXPRESS

References

1. K. H. Song, E. W. Stein, J. A. Margenthaler, and L. V. Wang, "Noninvasive photoacoustic identification of sentinel lymph nodes containing methylene blue in vivo in a rat model," J. Biomed. Opt. **13**(5), 054033 (2008).
2. Q. R. J. G. Tummers, F. P. R. Verbeek, B. E. Schaafsma, M. C. Boonstra, J. R. van der Vorst, G. J. Liefers, C. J. H. van de Velde, J. V. Frangioni, and A. L. Vahrmeijer, "Real-time intraoperative detection of breast cancer using near-infrared fluorescence imaging and Methylene Blue," Eur J. Surg. Onc. (EJSO) **40**(7), 850–858 (2014).
3. S. Ngamruengphong, V. K. Sharma, and A. Das, "Diagnostic yield of methylene blue chromoendoscopy for detecting specialized intestinal metaplasia and dysplasia in Barrett's esophagus: a meta-analysis," Gastrointest. Endosc. **69**(6), 1021–1028 (2009).
4. K. D. Rao, M. A. Choma, S. Yazdanfar, A. M. Rollins, and J. A. Izatt, "Molecular contrast in optical coherence tomography by use of a pump-probe technique," Opt. Lett. **28**(5), 340–342 (2003).
5. W. Kim and B. E. Applegate, "In vivo molecular contrast OCT imaging of methylene blue," Opt. Lett. **40**(7), 1426–1429 (2015).
6. J. Davies, D. Burke, J. R. Olliver, L. J. Hardie, C. P. Wild, and M. N. Routledge, "Methylene blue but not indigo carmine causes DNA damage to colonocytes in vitro and in vivo at concentrations used in clinical chromoendoscopy," Gut **56**(1), 155–156 (2007).
7. M. Oz, D. E. Lorke, M. Hasan, and G. A. Petroianu, "Cellular and molecular actions of Methylene Blue in the nervous system," Med. Res. Rev. **31**(1), 93–117 (2011).
8. T. Gambichler, G. Moussa, M. Sand, D. Sand, P. Altmeyer, and K. Hoffmann, "Applications of optical coherence tomography in dermatology," J. Dermatol. Sci. **40**(2), 85–94 (2005).
9. F. Prati, E. Regar, G. S. Mintz, E. Arbustini, C. Di Mario, I. K. Jang, T. Akasaka, M. Costa, G. Guagliumi, E. Grube, Y. Ozaki, F. Pinto, and P. W. Serruys, O. C. T. R. D. Expert's, "Expert review document on methodology, terminology, and clinical applications of optical coherence tomography: physical principles, methodology of image acquisition, and clinical application for assessment of coronary arteries and atherosclerosis," Eur. Heart J. **31**(4), 401–415 (2010).
10. M. Adhi and J. S. Duker, "Optical coherence tomography–current and future applications," Curr. Opin. Ophthalmol. **24**(3), 213–221 (2013).
11. G. Isenberg, M. V. Sivak Jr., A. Chak, R. C. Wong, J. E. Willis, B. Wolf, D. Y. Rowland, A. Das, and A. Rollins, "Accuracy of endoscopic optical coherence tomography in the detection of dysplasia in Barrett's esophagus: a prospective, double-blinded study," Gastrointest. Endosc. **62**(6), 825–831 (2005).
12. J. G. Fujimoto, C. Pitris, S. A. Boppart, and M. E. Brezinski, "Optical coherence tomography: An emerging technology for biomedical imaging and optical biopsy," Neoplasia **2**(1-2), 9–25 (2000).
13. J. Kim, W. Brown, J. R. Maher, H. Levinson, and A. Wax, "Functional optical coherence tomography: principles and progress," Phys. Med. Biol. **60**(10), R211–R237 (2015).
14. B. E. Applegate, C. H. Yang, and J. A. Izatt, "Theoretical comparison of the sensitivity of molecular contrast optical coherence tomography techniques," Opt. Express **13**(20), 8146–8163 (2005).
15. D. Jacob, R. L. Shelton, and B. E. Applegate, "Fourier domain pump-probe optical coherence tomography imaging of Melanin," Opt. Express **18**(12), 12399–12410 (2010).
16. M. J. Heslinga, E. M. Mastria, and O. Eniola-Adefeso, "Fabrication of biodegradable spheroidal microparticles for drug delivery applications," J. Controlled Release **138**(3), 235–242 (2009).
17. C. Cannava, R. Stancanelli, M. R. Marabeti, V. Venuti, C. Cascio, P. Guarneri, C. Bongiorno, G. Sortino, D. Majolino, A. Mazzaglia, S. Tommasini, and C. A. Ventura, "Nanospheres based on PLGA/amphiphilic cyclodextrin assemblies as potential enhancers of Methylene Blue neuroprotective effect," RSC Adv. **6**(20), 16720–16729 (2016).
18. V. Klepac-Ceraj, N. Patel, X. Song, C. Holewa, C. Patel, R. Kent, M. M. Amiji, and N. S. Soukos, "Photodynamic effects of methylene blue-loaded polymeric nanoparticles on dental plaque bacteria," Lasers Surg. Med. **43**(7), 600–606 (2011).
19. M. E. Keegan, J. L. Falcone, T. C. Leung, and W. M. Saltzman, "Biodegradable microspheres with enhanced capacity for covalently bound surface ligands," Macromolecules **37**(26), 9779–9784 (2004).
20. M. Qin, H. J. Hah, G. Kim, G. Nie, Y. E. Lee, and R. Kopelman, "Methylene blue covalently loaded polyacrylamide nanoparticles for enhanced tumor-targeted photodynamic therapy," Photochem. Photobiol. Sci. **10**(5), 832–841 (2011).
21. W. Tang, H. Xu, E. J. Park, M. A. Philbert, and R. Kopelman, "Encapsulation of methylene blue in polyacrylamide nanoparticle platforms protects its photodynamic effectiveness," Biochem. Biophys. Res. Commun. **369**(2), 579–583 (2008).
22. X. He, X. Wu, K. Wang, B. Shi, and L. Hai, "Methylene blue-encapsulated phosphonate-terminated silica nanoparticles for simultaneous in vivo imaging and photodynamic therapy," Biomaterials **30**(29), 5601–5609 (2009).
23. H. Sakai, B. Li, W. L. Lim, and Y. Iga, "Red blood cells donate electrons to methylene blue mediated chemical reduction of methemoglobin compartmentalized in liposomes in blood," Bioconjugate Chem. **25**(7), 1301–1310 (2014).
24. G. Schafer and H. S. Penefsky, "Bioenergetics: energy conservation and conversion . Introduction," Results Probl. Cell Differ. **45**, IV–VIII (2008).
25. P. Charoenphol, S. Mocherla, D. Bouis, K. Namdee, D. J. Pinsky, and O. Eniola-Adefeso, "Targeting therapeutics to the vascular wall in atherosclerosis–carrier size matters," Atherosclerosis **217**(2), 364–370 (2011).

Biomedical Optics EXPRESS

26. P. Charoenphol, R. B. Huang, and O. Eniola-Adefeso, "Potential role of size and hemodynamics in the efficacy of vascular-targeted spherical drug carriers," Biomaterials **31**(6), 1392–1402 (2010).
27. O. Carrasco-Zevallos, R. L. Shelton, W. Kim, J. Pearson, and B. E. Applegate, "In vivo pump-probe optical coherence tomography imaging in Xenopus laevis," J. Biophotonics **8**(1-2), 25–35 (2015).
28. H. Y. Lee, P. D. Raphael, J. Park, A. K. Ellerbee, B. E. Applegate, and J. S. Oghalai, "Noninvasive in vivo imaging reveals differences between tectorial membrane and basilar membrane traveling waves in the mouse cochlea," Proc. Natl. Acad. Sci. U. S. A. **112**(10), 3128–3133 (2015).
29. J. B. Dewey, B. E. Applegate, and J. S. Oghalai, "Amplification and Suppression of Traveling Waves along the Mouse Organ of Corti: Evidence for Spatial Variation in the Longitudinal Coupling of Outer Hair Cell-Generated Forces," J. Neurosci. **39**(10), 1805–1816 (2019).
30. J. Park, E. F. Carbajal, X. Chen, J. S. Oghalai, and B. E. Applegate, "Phase-sensitive optical coherence tomography using an Vernier-tuned distributed Bragg reflector swept laser in the mouse middle ear," Opt. Lett. **39**(21), 6233–6236 (2014).
31. W. Kim, S. Kim, S. N. Huang, J. S. Oghalai, and B. E. Applegate, "Picometer scale vibrometry in the human middle ear using a surgical microscope based optical coherence tomography and vibrometry system," Biomed. Opt. Express **10**(9), 4395–4410 (2019).
32. J. M. Tarbell, "Shear stress and the endothelial transport barrier," Cardiovasc. Res. **87**(2), 320–330 (2010).
33. Y. Kim, M. E. Lobatto, T. Kawahara, B. Lee Chung, A. J. Mieszawska, B. L. Sanchez-Gaytan, F. Fay, M. L. Senders, C. Calcagno, J. Becraft, M. Tun Saung, R. E. Gordon, E. S. Stroes, M. Ma, O. C. Farokhzad, Z. A. Fayad, W. J. Mulder, and R. Langer, "Probing nanoparticle translocation across the permeable endothelium in experimental atherosclerosis," Proc. Natl. Acad. Sci. U. S. A. **111**(3), 1078–1083 (2014).
34. N. C. Chesler and O. C. Enyinna, "Particle deposition in arteries ex vivo: effects of pressure, flow, and waveform," J. Biomech. Eng. **125**(3), 389–394 (2003).
35. D. Gabrielli, E. Belisle, D. Severino, A. J. Kowaltowski, and M. S. Baptista, "Binding, aggregation and photochemical properties of methylene blue in mitochondrial suspensions," Photochem. Photobiol. **79**(3), 227–232 (2004).
36. D. Severino, H. C. Junqueira, M. Gugliotti, D. S. Gabrielli, and M. S. Baptista, "Influence of negatively charged interfaces on the ground and excited state properties of methylene blue," Photochem. Photobiol. **77**(5), 459–468 (2003).
37. E. Morgounova, Q. Shao, B. J. Hackel, D. D. Thomas, and S. Ashkenazi, "Photoacoustic lifetime contrast between methylene blue monomers and self-quenched dimers as a model for dual-labeled activatable probes," J. Biomed. Opt. **18**(5), 056004 (2013).
38. J. P. Tardivo, A. Del Giglio, C. S. de Oliveira, D. S. Gabrielli, H. C. Junqueira, D. B. Tada, D. Severino, R. de Fatima Turchiello, and M. S. Baptista, "Methylene blue in photodynamic therapy: From basic mechanisms to clinical applications," Photodiagn. Photodyn. Ther. **2**(3), 175–191 (2005).
39. B. E. Applegate and J. A. Izatt, "Molecular imaging of endogenous and exogenous chromophores using ground state recovery pump-probe optical coherence tomography," Opt. Express **14**(20), 9142–9155 (2006).
40. I. D. Rosca, F. Watari, and M. Uo, "Microparticle formation and its mechanism in single and double emulsion solvent evaporation," J. Controlled Release **99**(2), 271–280 (2004).
41. N. Sharma, P. Madan, and S. S. Lin, "Effect of process and formulation variables on the preparation of parenteral paclitaxel-loaded biodegradable polymeric nanoparticles: A co-surfactant study," Asian J. Pharm. Sci. **11**(3), 404–416 (2016).
42. S. Mao, Y. Shi, L. Li, J. Xu, A. Schaper, and T. Kissel, "Effects of process and formulation parameters on characteristics and internal morphology of poly(d,l-lactide-co-glycolide) microspheres formed by the solvent evaporation method," Eur. J. Pharm. Biopharm. **68**(2), 214–223 (2008).
43. A. Budhian, S. J. Siegel, and K. I. Winey, "Haloperidol-loaded PLGA nanoparticles: systematic study of particle size and drug content," Int. J. Pharm. **336**(2), 367–375 (2007).
44. X. Song, Y. Zhao, W. Wu, Y. Bi, Z. Cai, Q. Chen, Y. Li, and S. Hou, "PLGA nanoparticles simultaneously loaded with vincristine sulfate and verapamil hydrochloride: systematic study of particle size and drug entrapment efficiency," Int. J. Pharm. **350**(1-2), 320–329 (2008).
45. G. S. Singhal and E. Rabinowi, "Changes in Absorption Spectrum of Methylene Blue with Ph," J. Phys. Chem. **71**(10), 3347–3349 (1967).
46. H. K. Makadia and S. J. Siegel, "Poly Lactic-co-Glycolic Acid (PLGA) as Biodegradable Controlled Drug Delivery Carrier," Polymers **3**(3), 1377–1397 (2011).
47. A. R. DiSanto and J. G. Wagner, "Pharmacokinetics of highly ionized drugs. II. Methylene blue–absorption, metabolism, and excretion in man and dog after oral administration," J. Pharm. Sci. **61**(4), 598–602 (1972).
48. J. M. May, Z. C. Qu, and C. E. Cobb, "Reduction and uptake of methylene blue by human erythrocytes," Am. J. Physiol. Cell Physiol. **286**(6), C1390–C1398 (2004).
49. R. W. Redmond and J. N. Gamlin, "A compilation of singlet oxygen yields from biologically relevant molecules," Photochem. Photobiol. **70**(4), 391–475 (1999).
50. M. C. DeRosa and R. J. Crutchley, "Photosensitized singlet oxygen and its applications," Coord. Chem. Rev. **233-234**, 351–371 (2002).
51. W. Tang, H. Xu, R. Kopelman, and M. A. Philbert, "Photodynamic characterization and in vitro application of methylene blue-containing nanoparticle platforms," Photochem. Photobiol. **81**(2), 242–249 (2005).

Biomedical Optics EXPRESS

52. H. J. Hah, G. Kim, Y. E. Lee, D. A. Orringer, O. Sagher, M. A. Philbert, and R. Kopelman, "Methylene blue-conjugated hydrogel nanoparticles and tumor-cell targeted photodynamic therapy," Macromol. Biosci. **11**(1), 90–99 (2011).
53. K. Orth, G. Beck, F. Genze, and A. Ruck, "Methylene blue mediated photodynamic therapy in experimental colorectal tumors in mice," J. Photochem. Photobiol., B **57**(2-3), 186–192 (2000).
54. C. W. Merkle, M. Augustin, D. J. Harper, and B. Baumann, "Indocyanine green provides absorption and spectral contrast for optical coherence tomography at 840 nm in vivo," Opt. Lett. **45**(8), 2359–2362 (2020).
55. P. Si, S. Shevidi, E. Yuan, K. Yuan, Z. Lautman, S. S. Jeffrey, G. W. Sledge, and A. de la Zerda, "Gold Nanobipyramids as Second Near Infrared Optical Coherence Tomography Contrast Agents for in Vivo Multiplexing Studies," Nano Lett. **20**(1), 101–108 (2020).
56. C. W. Merkle and V. J. Srinivasan, "Laminar microvascular transit time distribution in the mouse somatosensory cortex revealed by Dynamic Contrast Optical Coherence Tomography," NeuroImage **125**, 350–362 (2016).
57. Y. Pan, J. You, N. D. Volkow, K. Park, and C. Du, "Ultrasensitive detection of 3D cerebral microvascular network dynamics in vivo," NeuroImage **103**, 492–501 (2014).
58. J. Zhang, J. Liu, L. M. Wang, Z. Y. Li, and Z. Yuan, "Retroreflective-type Janus microspheres as a novel contrast agent for enhanced optical coherence tomography," J. Biophotonics **10**(6-7), 878–886 (2017).
59. Y. Yeo and K. N. Park, "Control of encapsulation efficiency and initial burst in polymeric microparticle systems," Arch. Pharmacal Res. **27**(1), 1–12 (2004).
60. N. V. Jyothi, P. M. Prasanna, S. N. Sakarkar, K. S. Prabha, P. S. Ramaiah, and G. Y. Srawan, "Microencapsulation techniques, factors influencing encapsulation efficiency," J. Microencapsulation **27**(3), 187–197 (2010).
61. R. Alex and R. Bodmeier, "Encapsulation of water-soluble drugs by a modified solvent evaporation method. I. Effect of process and formulation variables on drug entrapment," J. Microencapsulation **7**(3), 347–355 (1990).
62. R. Bonnett, "Photosensitizers of the Porphyrin and Phthalocyanine Series for Photodynamic Therapy," Chem. Soc. Rev. **24**(1), 19–33 (1995).
63. A. Phinikaridou, M. E. Andia, A. Protti, A. Indermuehle, A. Shah, A. Smith, A. Warley, and R. M. Botnar, "Noninvasive magnetic resonance imaging evaluation of endothelial permeability in murine atherosclerosis using an albumin-binding contrast agent," Circulation **126**(6), 707–719 (2012).
64. J. M. Lu, X. Wang, C. Marin-Muller, H. Wang, P. H. Lin, Q. Yao, and C. Chen, "Current advances in research and clinical applications of PLGA-based nanotechnology," Expert Rev. Mol. Diagn. **9**(4), 325–341 (2009).